

Dynamics of Intensified Downwelling Circulation over a Widened Shelf in the Northeastern South China Sea

JIANPING GAN, HO SAN HO, AND LINLIN LIANG

Division of Environment, and Department of Mathematics, Hong Kong University of Science and Technology, Hong Kong, China

(Manuscript received 4 January 2012, in final form 9 August 2012)

ABSTRACT

This study reveals the dynamics behind the intensified, downslope, cross-isobath transport over a widened shelf (narrowing downwave) in the northeastern South China Sea (NSCS) during a downwelling event. Utilizing a three-dimensional numerical model over an idealized NSCS shelf, this study identified the forcing process and derived an analytical understanding of the invoked dynamics for the intensified downslope cross-isobath transport. This study found that the transport was formed by an amplified geostrophic transport because of an increased positive along-isobath pressure gradient force (PGF), PY^* , and by an enhanced bottom Ekman transport due to converging flow over the widened shelf. Based on the depth-integrated vorticity dynamics, PY^* was linked with net frictional stress curl in the water column and the curl was primarily associated with the shear vorticity field induced by downwelling jet. The increased positive vorticity seaside of the jet provided positive PY^* for the downslope geostrophic transport. The cross-isobath PGF, PX^* , which was geostrophically formed and shaped by the spatially asymmetric isobaths of the widened shelf, determined the intensities of the jet and thus the associated shear vorticity that quantified the respective bottom friction transport and PY^* for the intensified cross-isobath transport. It was found that the downslope transport over the widened shelf was strengthened in a stratified flow by the linked intensifications of barotropic PX^* or the concurrent downwelling jet, shear vorticity field, PY^* , and bottom friction because of an increase of volume flux upstream of the widened shelf.

1. Introduction

Wind-driven coastal downwelling over the continental shelf has been generally described as two-dimensional circulation in which water mass piles up against the coast because of surface Ekman transport. It forms a geostrophic coastal jet and a compensating seaward bottom Ekman transport. The cross-shelf gradient of isobaths over the shelf tightly controls the intensity of the alongshore flow and the ensuing cross-shore bottom friction transport in the two-dimensional downwelling paradigm (Allen and Newberger 1996). Although the theory of cross-shelf, two-dimensional circulation is the basis of the fundamental dynamics for coastal downwelling circulation, it neglects the coastal dynamics in the alongshore direction and is dynamically insufficient to depict the cross-shelf transport over a variable shelf. More

and more studies have shown that a three-dimensional coastal circulation can deviate substantially from a two-dimensional flow regime in which variable shelf topography in the alongshore direction greatly constrains the orientation of alongshore flow and geostrophically modulates the intensity of the cross-shelf transport (e.g., Lentz et al. 1999; Gan and Allen 2002; Weisberg et al. 2005). Based on the zeroth-order solution of barotropic dynamics, Janowitz and Pietrafesa (1982) showed that diverging shelf isobaths produced a variation in the vorticity and led to the formation of a vertical vorticity as well as a cross-isobath flow. However, their assumption of the nonlinear advection, instead of friction, in the ageostrophic momentum balance is not consistent with the realistic dynamics in the shelf sea. From the steady, linear barotropic potential vorticity dynamics, Pringle (2002) provided the dynamic interpretation for the enhanced onshore cross-isobath transport in the upwelling circulation over a shelf narrowing in the direction of long coastal trapped wave (defined as the widened shelf in this study). He also showed the absence of enhanced cross-isobath transport of downwelling circulation in

Corresponding author address: Jianping Gan, Division of Environment and Department of Mathematics, Hong Kong University of Science and Technology, Hong Kong, China.
E-mail: magan@ust.hk

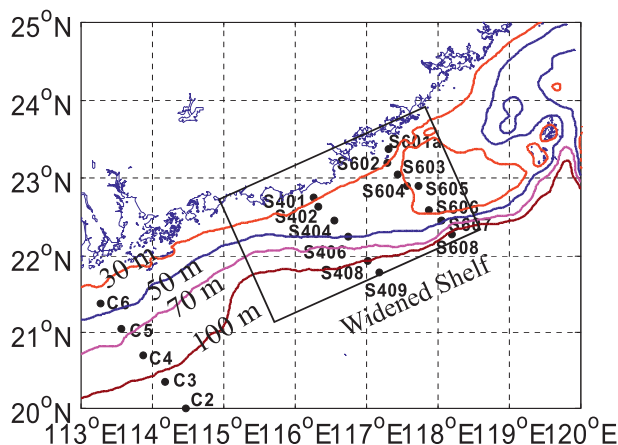


FIG. 1. Bathymetry and the CTD sampling stations in the NSCS. The solid circles are CTD stations and the red, blue, purple, and brown contour lines are the 30-, 50-, 75-, and 100-m isobaths, respectively. The widened shelf is between 115.5° and 118°E.

a shelf that widens downwave. Based on observational and three-dimensional modeling studies, Gan et al. (2009a) also found an intensified upslope cross-isobath transport of upwelling circulation over a widened shelf. Although previous studies have identified the enhanced cross-isobath geostrophic and bottom frictional transports as the major contributors to the intensified cross-shelf transport over the widened shelf, many of its dynamical rationalization remain unclear. For example, solidly based explanations for the nature and origin of the force that drives the enhanced cross-isobath geostrophic transport and the response of the transport in stratified flow have not been provided. In addition, most of the previous studies mainly focused on the wind-driven upwelling shelf circulation. The cross-isobath transport in the coastal downwelling circulation that is not a complete asymmetric response to the upwelling circulation has not been adequately discussed.

We were motivated in this current study by the observed evidence of the intensified downslope cross-shelf transport over a widened shelf in the northeastern South China Sea (NSCS, Fig. 1). The widened shelf is characterized by the existence of a prominent eastward widening that is indicated by an abrupt offshore extension of the 50-m isobath east of the 115°E. In winter and fall, the prevailing northeasterly downwelling favorable monsoon forms coastal downwelling circulation over the NSCS shelf. The near-shore water of the NSCS is cooled by the corresponding southwestward advection of colder coastal water from the East China Sea. This cooler water extends offshore over the widened shelf, but it is constrained shoreward around the 50-m isobath (Fig. 2). Three conductivity–temperature–depth (CTD) cross-shelf transects (lines C, S4, and S6 in Fig. 1) were

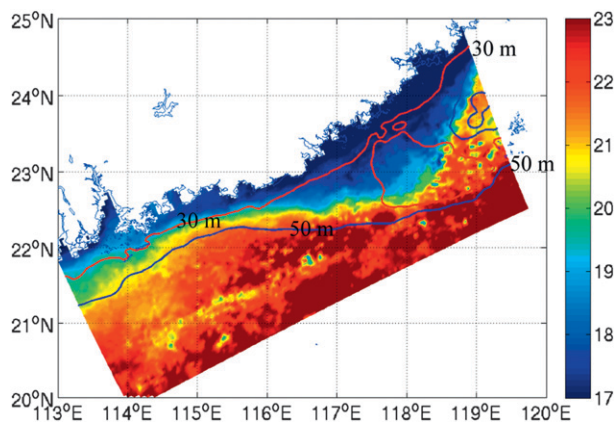


FIG. 2. Moderate Resolution Imaging Spectroradiometer (MODIS) sea surface temperatures (SST, °C) averaged during a cruise in 2009. The red and blue contours are the 30- and 50-m isobaths, respectively.

performed during the winter of 2008 and the fall of 2011, and the data showed the strong alongshore variability of the cross-shelf transport (Fig. 3). An intensified seaward, downslope, cross-isobath transport of the shelf water distinctly occurred along transect S4 over the widened shelf. This strong transport created vertically stratified bottom water underneath the well-mixed water column above. Similar conditions were absent from the two other transects (lines C and S6) away from the widened shelf where the water columns were vertically uniform and low/high temperatures were located in near-shore/offshore waters, respectively. The intensified seaward cross-shelf transport over the widened shelf in NSCS that narrows downwave is a robust coastal phenomenon that has never been reported. In this study, we examine the forcing process and underlying dynamics of wind-driven downwelling circulation over the NSCS widened shelf, based on the result of a three-dimensional numerical model.

2. Ocean model

The ocean model that we used was the Regional Ocean Modeling System (ROMS) (Shchepetkin and McWilliams 2005) for three-dimensional, time-dependent flows governed by hydrostatic primitive equations. We adopted a local closure scheme in the vertical mixing parameterization that was based on the level-2.5 turbulent kinetic energy equations by Mellor and Yamada (1982). To extract and identify fundamental dynamic response to various physical forcing such as topography and stratification, we first utilized the barotropic mode of the ROMS with a vertically nonstratified water column, and, subsequently, a baroclinic mode with a vertically stratified water column over an idealized widened

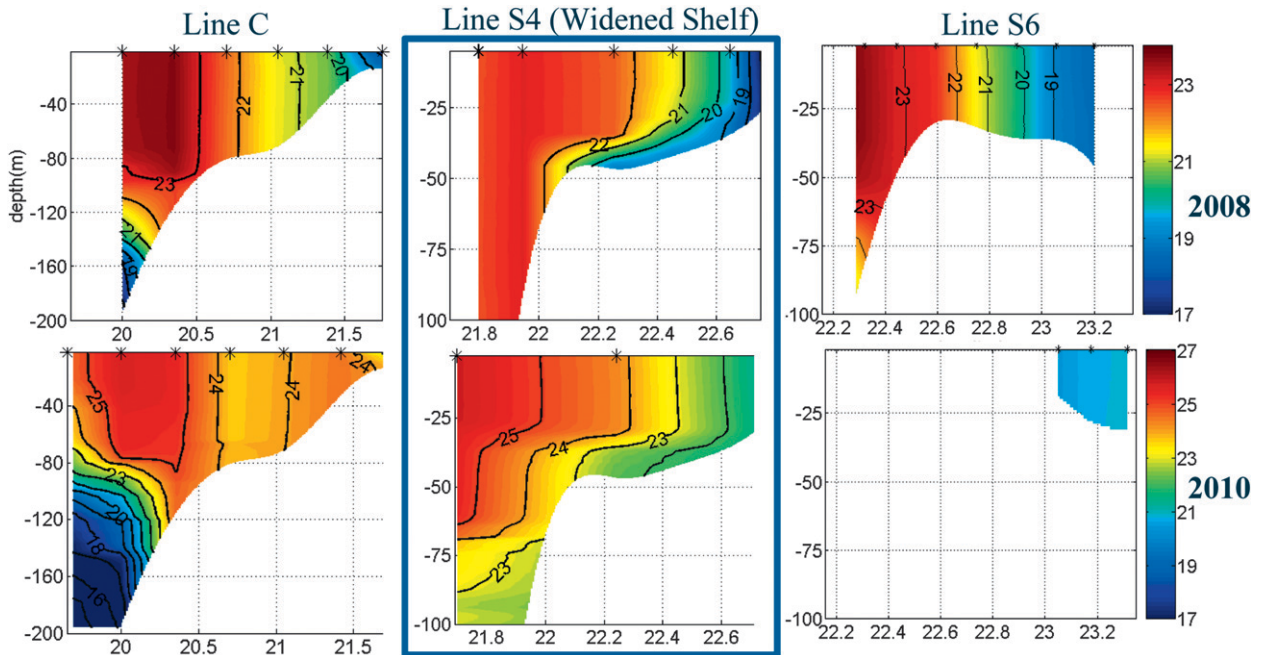


FIG. 3. CTD cross-shelf transects of temperature ($^{\circ}\text{C}$) along line C off the Pearl River Estuary, line S4 across the widened shelf, and line S6 over Taiwan Shoals (see Fig. 1), forced by northeasterly downwelling favorable winds in (top) the winter of 2008 and (bottom) the fall of 2010. Compared to lines C and S6, line S4 distinctly shows an intensified seaward cross-isobath over the widened shelf.

shelf (Fig. 4). The idealized widened shelf is chosen to mimic the one in the NSCS (Fig. 1) and to specifically focus on the fundamental process of cross-isobath transport over a widened shelf. The shelf width was 66 km at the western end and it gradually widened to 152 km at its eastern end. The water depth linearly increased from 10 m at the coast to the 200-m isobath offshore where we defined the isobath to be parallel to the coastline. The water depth then continues to increase to the maximum water depth of 1000 m in the domain. Both the length and the width of the idealized shelf (shown by the rectangular box in Fig. 4) are analogous to the NSCS widened shelf between 115° and 117.5°E (Fig. 1). The computational model domain extended farther westward about 300 km from the existing western boundary of the NSCS widened shelf. To apply a cyclic boundary condition at the eastern and western boundaries, the width of the shelf increased linearly from the existing 66 to 152 km over additional westward extended shelf of 200 km (the portion is not shown in Fig. 4), such that the shelf topography in the western boundary completely matched that of the eastern boundary. For limited time integration, the cyclic boundary condition can be approximately treated as a “well-defined” solution (Gan et al. 2005). The extended artificial shelf, which allows the utilization of cyclic condition, is long enough such that any possible spurious signal has a minimized effect on the widened shelf. We found that the model solution was

quasi two-dimensional ~ 50 km in the upwave and ~ 350 km in the downwave directions of the concerned widened shelf. A radiation condition is used at the southern open boundary. The grid size was 3 km in the cross-shore and alongshore directions. In the case of the stratified water column, we adopted stretched generalized terrain-following coordinate with 30 levels in the vertical direction. Higher vertical resolution was distributed at the surface (grid size < 1 m) and bottom (grid size < 1.5 m) boundary layers over the widened shelf, respectively.

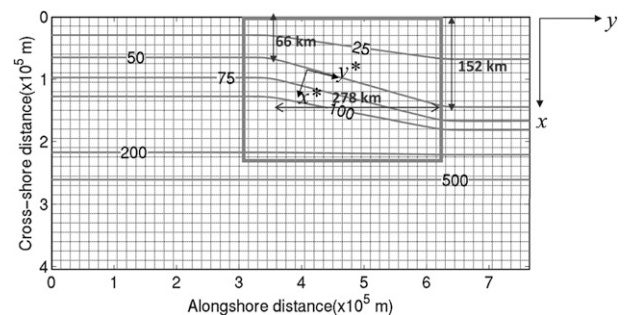


FIG. 4. Model grid with an embedded widened shelf (green rectangular box) that mimics the region in the northeastern South China Sea. (x, y) are the alongshore coordinates and (x^*, y^*) are the along-isobath coordinates. The computational domain extended westward 300 km from the existing western boundary such that cyclic boundary conditions could be applied in the western and eastern open boundaries. The grid size is 3 km.

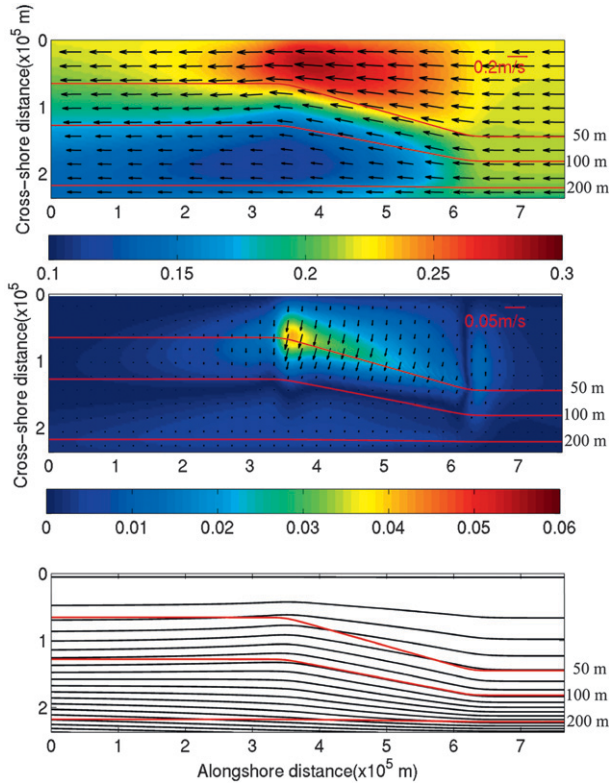


FIG. 5. (top to bottom) Depth-averaged velocity vectors and their magnitudes (m s^{-1} , color contours); depth-averaged velocity vectors normal to the isobaths and their magnitudes (m s^{-1} , color contours); and barotropic streamlines (contour interval: $-2 \times 10^{-5} \text{ m}^3 \text{ s}^{-1}$) for nonstratified flow on day 15.

In this process-oriented study of the downwelling circulation, we forced the model with a spatially uniform northeasterly wind stress (0.1 Pa) that represented the winter northeasterly wind stress in the NSCS. In the stratified case, we initialized the model with horizontally uniform *World Ocean Atlas* (WOA) temperature and salinity profiles from about 150-m depth off Hong Kong. For simplicity, we set atmospheric heat and buoyancy fluxes to zero. The model was spun up from a motionless ocean until it reached a quasi-steady state in ~ 13 days.

3. Barotropic dynamics

a. Barotropic circulation

The characteristic responses of downwelling circulation over a nonstratified shelf are shown in Fig. 5. Forced by a downwelling favorable wind, surface Ekman drift geostrophically established a westward coastal downwelling jet. Stronger shelf currents occurred over the shallower water shoreward of the 50-m isobath and the weaker currents existed in the deeper waters off the widened shelf.

The strongest (weakest) currents appeared shoreward (seaward) of the 50-m isobath near the head of the widened shelf because of converging (diverging) currents that followed the local isobaths. Meanwhile, substantial deviation of currents from isobaths occurred over the widened shelf. A relatively large deviation between the isobaths and streamlines occurred over the widened shelf along the 50-m isobath. A band of that intensified seaward transport elongated roughly along the direction of the 50-m isobath and decreased from a maximum value at the head toward the tail. The widened shelf region was distinct from the rest of the shelf because of this unique intensified seaward transport that was analogous to the results inferred from the field measurements.

b. Barotropic potential vorticity dynamics

The underlying dynamics for the intensified seaward transport over the widened shelf can be illustrated by a steady, barotropic PV dynamics:

$$J\left(\frac{f + \zeta}{H}, \Psi\right) + \nabla \times \left(\frac{\tau_s}{\rho_0 H}\right) - \nabla \cdot \left(\frac{c_d \|\nabla \Psi\|}{H^3} \nabla \Psi\right) = 0, \quad (1)$$

where J is the Jacobian determinant, Ψ is the transport streamfunction, and $U = -\Psi_y$ and $V = \Psi_x$. Here, U and V are depth-integrated across-shelf and along-shelf velocities, respectively, τ_s is the surface stress, H is water depth, ρ_0 is the reference density, c_d is the frictional drag coefficient, and f and ζ are planetary and vertical components of the relative vorticity, respectively. The last term in the left side is the curl of bottom stress term when a quadratic drag law is applied and the near-bottom velocity is set to be the depth-integrated velocity divided by the water depth. Equation (1) states that the advection of absolute vorticity is balanced by the input of both the PV from wind stress curl $\nabla \times [\tau_s / (\rho_0 H)]$ and the dissipation of vorticity due to friction $-\nabla \cdot [(c_d \|\nabla \Psi\| / H^3) \nabla \Psi]$.

Figure 6 shows the term balance of Eq. (1) on day 15 over the widened shelf. As expected from the flow field in Fig. 5, PV advection was relatively small away from the widened shelf where isobaths and streamlines coincide. The negative residual between $-\nabla \cdot [(c_d \|\nabla \Psi\| / H^3) \nabla \Psi]$ and $\nabla \times [\tau_s / (\rho_0 H)]$ balanced the positive PV advection term; it suggested that the net frictional removal of PV lowered the positive PV to the seaside of the downwelling jet and veered the flow offshore. When the Rossby number is small, we can illustrate the cross-isobath transport better by expressing the PV advection term with rotated rectangular coordinates (x^* , y^*), in which y^* is along the isobaths and is positive eastward

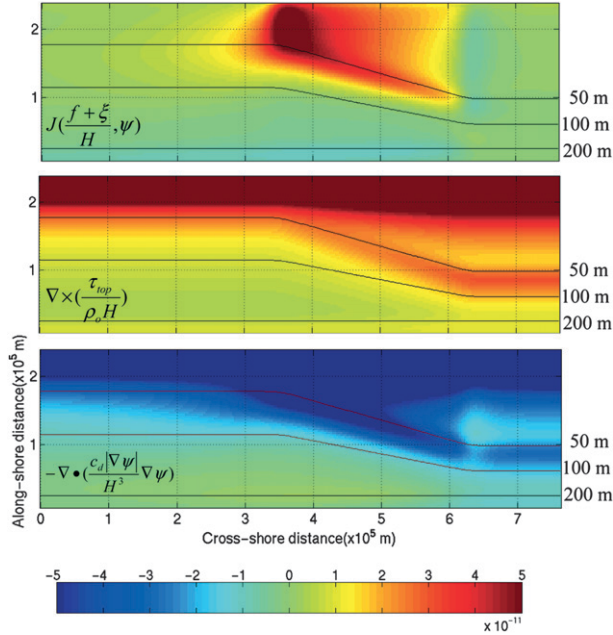


FIG. 6. (top to bottom) Advection of absolute vorticity, the input of potential vorticity from wind stress curl and the dissipation of vorticity by friction in the barotropic potential vorticity equation for nonstratified flow on day 15 ($\text{s}^{-2} \text{m}^{-1}$).

(Fig. 4). The coordinate x^* is normal to the isobaths and directs offshore. Thus,

$$J\left(\frac{f}{H}, \Psi\right) = \frac{\partial \Psi}{\partial y^*} \frac{\partial}{\partial x^*} \left(\frac{f}{H}\right) = -U^* \frac{\partial}{\partial x^*} \left(\frac{f}{H}\right). \quad (2)$$

Here, U^* is the velocity normal to the isobaths and is positive seaward. As shown in Fig. 6, Eq. (2) > 0 in the f plane during downwelling, and

$$-U^* \frac{\partial}{\partial x^*} \left(\frac{f}{H}\right) = U^* \frac{f}{H^2} \frac{\partial H}{\partial x^*} > 0. \quad (3)$$

Because $\partial H / \partial x^* = H_{x^*} > 0$, $U^* > 0$ directed seaward across the isobaths or

$$U^* = \frac{H^2 \left[\nabla \cdot \left(\frac{c_d \|\nabla \Psi\|}{H^3} \nabla \Psi \right) - \nabla \times \frac{\tau_s}{\rho_o H} \right]}{f H_{x^*}}. \quad (4)$$

Equation (4) shows that seaward cross-isobath transport is induced by frictional removal of PV when the wind stress curl is absent.

c. Nonlinearity and component contribution

Because the current detoured around the widened shelf, it may be useful to examine the effect of nonlinearity on the flow variation. By subtracting the results of the model case without nonlinear advection from the one

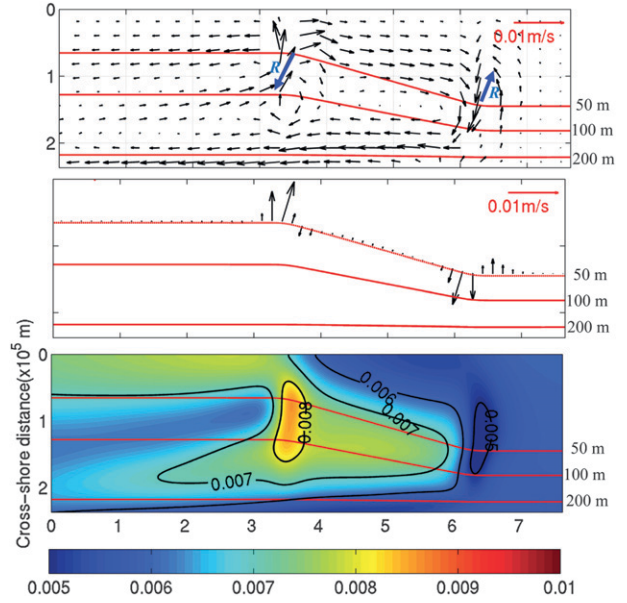


FIG. 7. (top to bottom) Differences of velocity vectors (m s^{-1}), velocity across the 50-m isobath (m s^{-1}) and surface elevation (m) between the cases with and without nonlinear advection terms for nonstratified flow on day 15. Blue arrows are the radius of curvature (R) of the streamline.

with it (Fig. 7), we found that it affected the flow field mainly at the head and tail of the widened shelf. However, the effect of nonlinear advection on the intensity of flow was very weak ($< 1 \text{ cm s}^{-1}$) in the entire domain. The effect of the nonlinear advection is expected to be amplified over the shelf with stronger curving isobaths. The gradient wind-like balance states

$$\frac{V_s^2}{R} + f V_s = -\frac{1}{\rho_o} \frac{\partial p}{\partial n}, \quad (5)$$

where \mathbf{n} is normal to the horizontal velocity and positive to the left of the flow direction; R is the radius of curvature of the streamlines and is positive in the direction of \mathbf{n} . Here, V_s is the along streamline velocity, and $\partial p / \partial n$ is the pressure gradient normal to the streamline. With dominant geostrophic current, we have $-(1/\rho_o)(\partial p / \partial n) > 0$. Because the flow tends to turn toward the left ($R > 0$) at the head and toward the right ($R < 0$) at the tail following the isobaths, locally amplified V_s^2/R due to small $\|R\|$ is positive and negative, respectively. Thus, according to Eq. (5), it tended to be balanced by an increasing $-(1/\rho_o)(\partial p / \partial n)$ at the head and by a decreasing one at the tail. This is equivalent to have a large surface elevation increase near the head where V_s is strong and a relatively small increase of surface elevation near the tail. The gradient of surface elevation change or $\nabla(\Delta \eta)$ induced by nonlinear advection then geostrophically

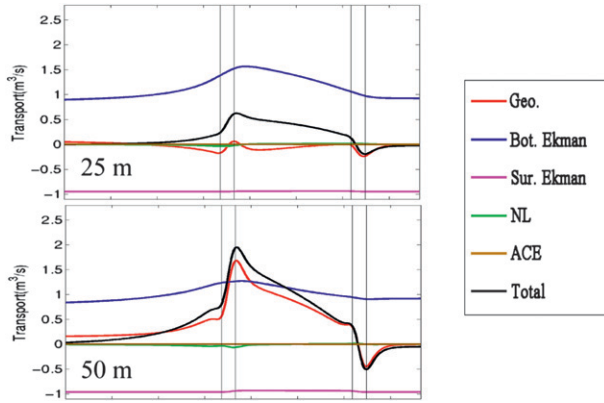


FIG. 8. Depth-integrated transports across the isobaths ($\text{m}^3 \text{s}^{-1}$) at (top) 25 m and (bottom) 50 m for nonstratified flow on day 15. Surface and bottom Ekman transports, nonlinear advection, and geostrophic currents contributed to the total transport. Positive values refer to the seaward transport. The areas between the two pairs of vertical solid lines are the locations of the head and tail of the widened shelf. The thin rectangular boxes mark the region extending 35 km from the head and tail.

formed a clockwise circulation over the widened shelf. The effect of nonlinear advection will be further illustrated by PV balance in section 5.

While the balance in Eq. (1) provides PV dynamics for the cross-isobath flow, the detailed dynamic processes involved in the flow–topography interaction for the intensified downslope transport over the widened shelf can be elaborated from the associated momentum balance. With a small contribution from nonlinearity, the total cross-isobath transport (T_t) was contributed by geostrophic current (T_g), surface (T_s) and bottom (T_b) Ekman transports. Figure 8 shows the contribution from each component along the 25- and 50-m isobaths, representing the respective conditions in the inner and outer parts of the widened shelf, and it displays considerable variation of T_t in both along- and cross-isobath directions.

Along the 25-m isobath, the seaward T_t amplified in the region of the widened shelf as bottom Ekman transport exceeded the surface Ekman transport in the horizontally converging flow over the widened shelf (see also Fig. 5). Here, T_g was generally small and negative, and thus $T_t < T_b$. Beyond the widened shelf, T_t was very weak because of the balance between the surface and bottom Ekman transport, and T_g was generally small while the currents mainly followed the isobaths. In the deeper waters, along the 50-m isobath, T_b was smaller than that in the near-shore waters over the widened shelf, but T_g increased substantially and contributed most to the net seaward transport over the widened shelf. The net positive (seaward) contribution of the frictional transport led to $T_t > T_g$. With the steep shelf at the head directly linking the shelf to the deep water, the intensified cross-isobath T_t effectively

moved the shelf water downslope into the deeper ocean as observed in NSCS (Fig. 3). The cross-shelf variation of T_g is associated with the corresponding variation of along-isobath pressures gradient force PY^* , which we know little about the dynamical rationalization for its formation.

4. Baroclinic downwelling transport

a. Development of downslope transport

The coastal downwelling circulation in the stratified shelf water behaved differently from that in the nonstratified case. Stratification may constrain the development of a bottom frictional layer over a sloping shelf because of the dynamics of arrested Ekman layers (MacCready and Rhines 1991), although the arrested bottom Ekman transport was not obvious in the highly variable alongshore topography of the widened shelf in this study. The stratification may modify the bottom boundary layer flow and flow above it by redistributing the buoyancy (Chapman and Lentz 1994, 1997). In our case, the baroclinicity strengthens the alongshore downwelling flow upstream due to weakening of the bottom frictional stress. This subsequently leads to an amplification of cross-shore transport of both T_g and T_b over the widened shelf (Fig. 9 and Section 5 below), while all fields qualitatively resembled those in Fig. 5.

Spatiotemporal variation of downwelling circulation in the stratified flow is illustrated by the cross-isobath density section along line A across the central part of the widened shelf and density section along the 50-m isobath on days 5 and 15 (Fig. 10). On day 5, the downslope density advection advanced gradually seaward, bended isopycnals downward to form a density front, leaving behind an inshore region of a relatively less-stratified water column. By day 15, the front reached a water depth of ~ 50 m at the edge of the widened shelf. Our results indicated that the front was trapped at the depth since day 10 and thereafter. The mechanism of the front trapping is likely caused by balance between the cross-shelf buoyancy flux and the vertical density diffusion, as a result of the modification of bottom boundary flow by density redistribution (Chapman and Lentz 1994, 1997).

In the along-isobath section, the seaward, downslope density advection formed a funnel-shaped less dense plume at the head of the widened shelf on day 5. This formed a positive and a negative along-isobath density gradient to the east and to the west of the plume, respectively. The subsequent arrival of the less dense water in the bottom layer on day 15 strengthened the stratification in the entire bottom layer on day 15. As a result of variation of cross-isobath velocity (u^*) along the isobaths (Fig. 9), and the variable shelf width, the magnitude of seaward density flux that reached the 50-m isobath

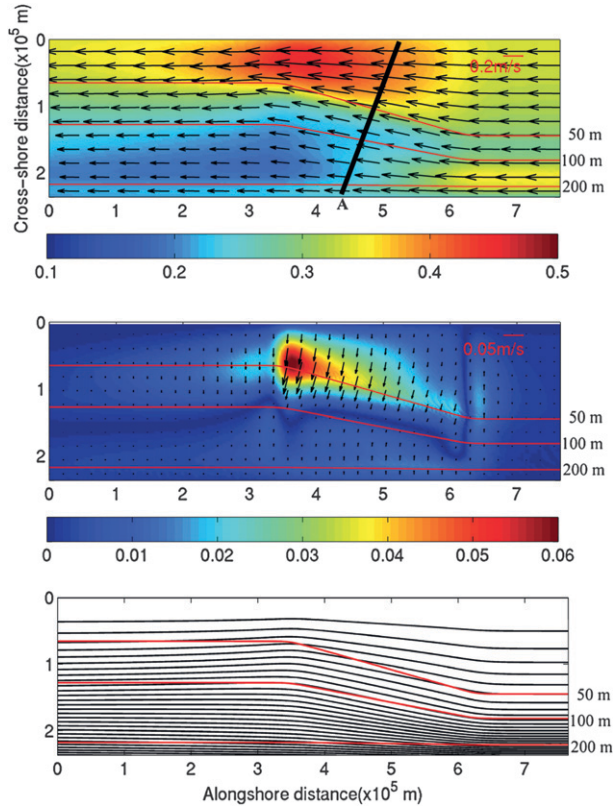


FIG. 9. (top to bottom) Depth-averaged velocity vectors (m s^{-1}) and their magnitudes (m s^{-1} , color contours); depth-averaged velocity vectors normal to the isobaths and their magnitudes (m s^{-1} , color contours); and barotropic streamlines for stratified flow on day 15. The thick line in the top panel refers to a cross-isobath line A in the central part of the widened shelf.

weakened from the head toward the tail. This formed an eastward uplifting of isopycnals or a negative barotropic along-isobath pressure gradient force. Although the geostrophic transport due to the variable cross-isobath density flux had a very limited effect on the cross-isobath transport in the case presented here, its effect may be amplified over the shelf with stronger alongshore variation.

b. Along-isobath momentum balance

The spatial variation of the cross-isobath transport over the widened shelf was governed by the corresponding variation in the balance of the along-isobath depth-dependent momentum balance

$$v_t^* = -\text{NL} - fu^* - \frac{1}{\rho} P_{y^*} + \text{HVIS} + \text{VVIS}, \quad (6)$$

where v_t^* refers to along-isobath velocity acceleration. The terms on the right side of Eq. (6) are nonlinear advection (NL), Coriolis force (COR), pressure gradient force (PGF), and horizontal (HVIS) and vertical (VVIS)

viscous terms. Subscript y^* represents the partial differentiation in the along-isobath direction. We may neglect the acceleration, NL, and HVIS terms since they are at least one order of magnitude smaller than the other terms and add $\text{AGE} = -fu^* - (1/\rho)P_{y^*}$ to assess the ageostrophy. Characteristics of v^* , u^* (or shown by $-\text{COR}$) and vertical velocity (w^*) are correlated with the corresponding balance of terms in Eq. (6) on day 15 (Fig. 11).

Here, v^* reached its maximum near the head of the widened shelf because of the confluence of current. It was vertically variable and decreased in both upstream and downstream from the head of the widened shelf, forming horizontal divergence/convergence upstream/downstream of the widened shelf. A downslope transport ($u^* > 0$ or $\text{COR} < 0$) formed in the bottom boundary layer to compensate for the onshore Ekman transport ($u^* < 0$ or $\text{COR} > 0$) in the surface layer. Similar to v^* , u^* varied along the isobath in the bottom boundary layer, and maximum u^* coincided with maximum v^* at the head of the widened shelf. Meanwhile, w^* had a very similar spatial structure to u^* , and the sinking ($w^* < 0$) in the bottom layer as $u^* > 0$ indicated a strong downslope transport over the widened shelf.

The balance of Eq. (6) along the isobath was mainly among the COR, PGF, and VVIS and exhibited a strong along-isobath variation. The prominent feature of the balance is highlighted by the existence of a barotropic positive along-isobath PGF (or PY^*) over the widened shelf that weakened gradually from a maximum value at the head to a smaller one at the tail. Here, PY^* geostrophically correlated with $u^* > 0$ in the entire water column over the widened shelf and contributed to a great portion of the cross-isobath transport over the widened shelf. The net transport between the surface and bottom boundary layers contributed to the remaining portion of cross-isobath transport, as indicated by the balance between VVIS and AGE. The frictional dynamics evidently determined the vertical structure of u^* in the boundary layers. VVIS weakened in the upper layer over the widened shelf as the alongshore current strengthened, because of the reduction of surface Ekman transport by the positive vorticity in the downwelling jet (Niller 1969).

5. Discussions and analyses

a. PGF

As shown, the intensified downslope cross-isobath transport was mainly contributed by the intensified geostrophic current (or PY^*) over the widened shelf, in both stratified and nonstratified flows. This cross-isobath geostrophic transport directed seaward on the seaside of the downwelling jet and shoreward on the shore-side of it (Figs. 5 and 8). The dynamical rationalization and

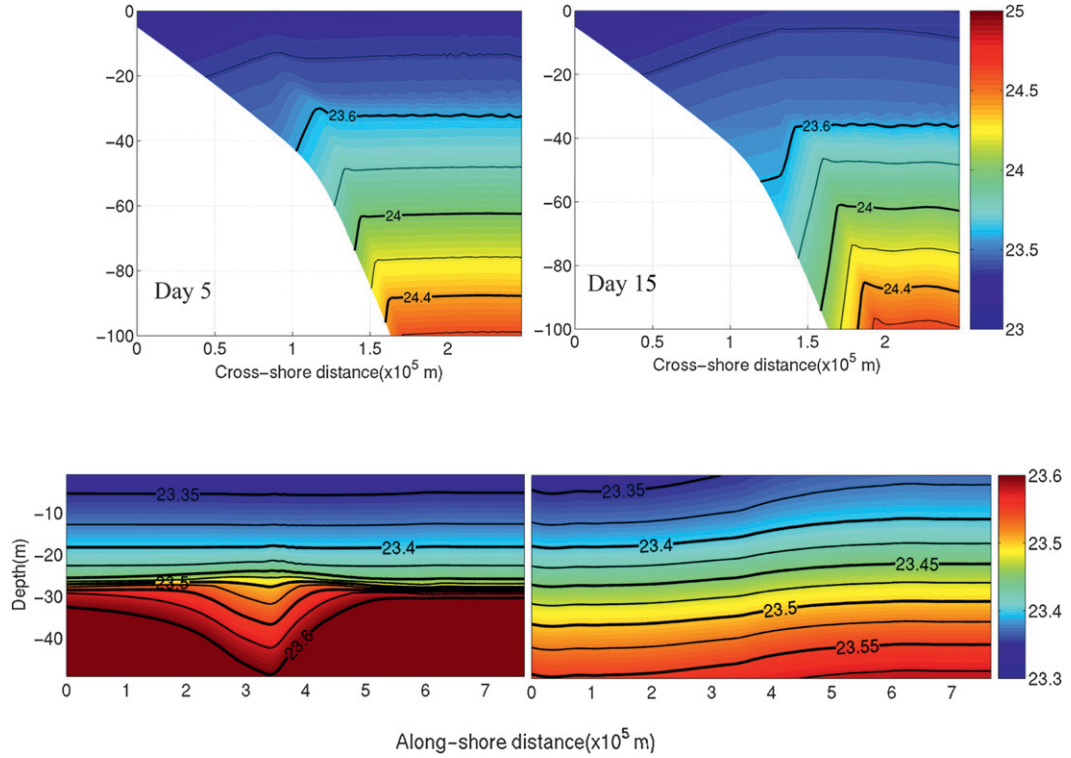


FIG. 10. (top) Cross-isobath section of σ_t (kg m^{-3}) along line A (Fig. 9) in the central part of the widened shelf, and (bottom) σ_t (kg m^{-3}) in the water column along the 50-m isobath in the stratified flow on days (left) 5 and (right) 15.

characteristics of PY^* over the widened shelf, thus, is crucial to identify the processes invoked in the intensified cross-isobath transport.

In the nonstratified flow, PY^* may be linked with net stress curl from the steady, linear depth-integrated vorticity equation (see appendix) as derived in the result of the geostrophic cross-isobath transport by Ho and Gan (2012, manuscript submitted to *J. Mar. Res.*)

$$\text{PYb}^* = -\frac{1}{\rho_o} P_{y^*}^b = \frac{\nabla \times \tau_b - \nabla \times \tau_s}{\rho_o H_{x^*}}, \quad (7)$$

where $P_{y^*}^b$ is the along-isobath bottom pressure gradient and PYb^* is the corresponding PGF or cross-isobath geostrophic transport. Equation (7) states that PYb^* was formed by the net stress curl in the water column. With the result of Eq. (7), the total cross-shore velocity in Eq. (4) can be readily expanded into the summation of bottom Ekman and geostrophic components. Under the quadratic drag law of bottom stress approximation, the bottom stress curl can be expressed as bottom vorticity or $\nabla \times \tau_b = \rho_o c_d (\nabla \times \|v_b\| v_b)$. Thus, when wind stress curl was absent as adopted in this study, Eq. (7) becomes

$$\text{PYb}^* = \frac{c_d (\nabla \times \|v_b\| v_b)}{H_{x^*}}, \quad (8)$$

and when curvature vorticity is small, it can be approximately by

$$\text{PYb}^* \approx \frac{2c_d \|v_b\| (\nabla \times v_b)}{H_{x^*}}, \quad (9)$$

where v_b is bottom velocity vector. Equation (8) or (9) states that the PYb^* is proportional to vertical stress shear or to bottom vorticity when wind stress curl is absent. This correlation is clearly illustrated by the similarity between the bottom vorticity in Fig. 12 and PYb^* Fig. 13. Since PGF was largely depth-independent (Fig. 11), $\text{PYb}^* \approx \text{PY}^*$, where PY^* is depth-integrated along-isobath PGF. In fact, it can be shown that PY^* is equal to PYb^* when density stratification is weak [see Eq. (12) below]. We found that the shear vorticity, rather than curvature vorticity, in the downwelling jet was the dominant vorticity that contributed to PY^* . Since shear vorticity in the jet was largely determined by the intensity of the jet, there was a clear connection between the magnitude of PY^* and the corresponding magnitude of cross-isobath PGF (PX^*), as to be shown below. In addition, since the vorticity in the jet, and, thus, PY^* , were induced by the widening of the shelf, their magnitudes are expected to increase when the degree of shelf wideness increases. The respective negative PY^* near-shore and

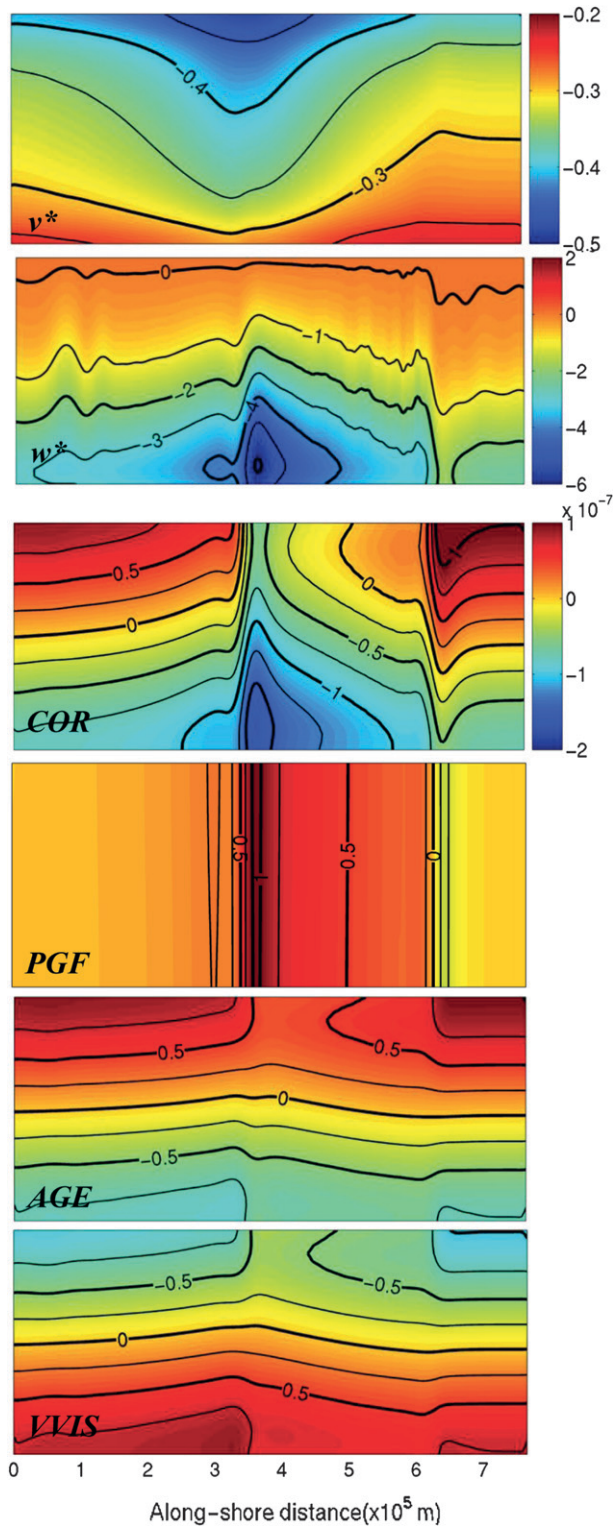


FIG. 11. (top to bottom) Velocity (v^* , m s^{-1}), vertical velocity (w^* , 10^{-5} m s^{-1}), and terms of COR, PGF, AGE, and VVIS (10^{-7} m s^{-2}) of Eq. (6) in the water column along the 50-m isobath for the stratified flow on day 15.

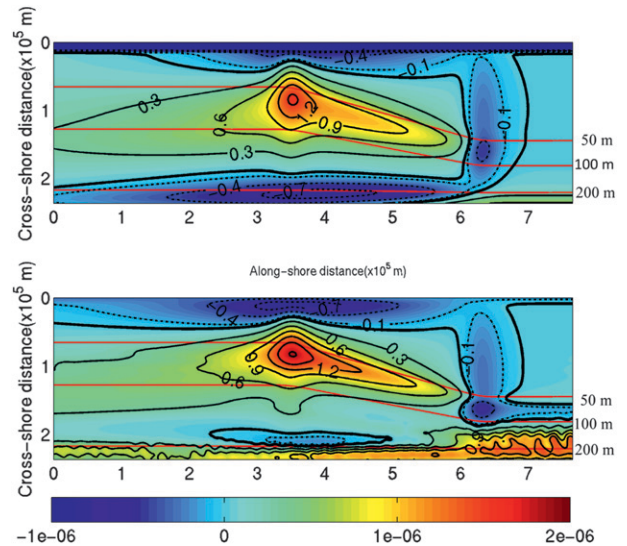


FIG. 12. (top) Bottom vorticity (10^{-6} s^{-1}) of the nonstratified flow and (bottom) bottom vorticity of the stratified flow on day 15. The red contour lines refer to the 50-, 100-, and 200-m isobaths.

positive PY^* offshore, roughly separated by the 30-m isobath (Fig. 13), were largely associated with the vorticity formed by the downwelling jet over the widened shelf (Fig. 12) and consistent with the cross-shelf variation of the cross-isobath geostrophic transport in Fig. 8. When wind stress curl was spatially uniform as in the case here, PYb^* (Fig. 13) was mainly balanced by bottom stress curl in Fig. 14, which greatly resembled the bottom vorticity. The $PY^* > 0$ elongated from the head of the widened shelf and decreased slowly toward the tail, but it weakened swiftly westward of the head. Away from the widened shelf, $\|PY^*\|$ was generally small.

When nonlinear advection was included, Eq. (7) becomes (also see appendix)

$$PYb^* = \frac{\nabla \times (\tau_b - \tau_s)}{\rho_o H_{x^*}} + \frac{1}{H_{x^*}} J(\Psi, \nabla \times V) + \frac{1}{2} (\|V^2\|)_{y^*}. \quad (10)$$

The second term on the right side of Eq. (10) is the contribution due to relative vorticity advection. The third term arises from the gradient of momentum flux and it forms alongshore pressure gradient for the irrotational ideal flow or

$$PYb^* = \frac{1}{2} (\|V^2\|)_{y^*}. \quad (11)$$

This effect may be important in deep water or where nonlinearity of flow is strong such as at the head and tail

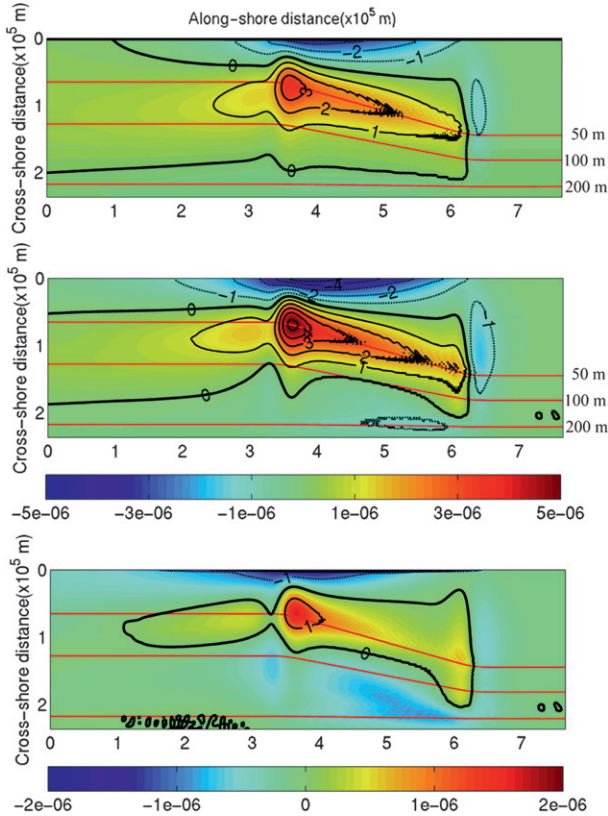


FIG. 13. Depth-integrated along-isobath pressure gradient force (PY^* , $10^{-6} \text{ m}^2 \text{ s}^{-2}$) in the (top) nonstratified, (middle) stratified flows, and (bottom) the difference between PY^* (stratified) and PY^* (non-stratified) on day 15.

of the widened shelf. It is, however, relatively small when friction is important.

In stratified flow, we have $PY_b^* \approx PY^*$ because of relatively well-mixed water over the widened shelf. PY^* is expected to be altered by The Joint Effect of Baroclinicity and Relief (JEBAR) term when flow is highly stratified. Figure 13 shows that PY^* in the stratified flow was qualitatively similar to the one in the nonstratified flow. Its magnitude, however, strengthened in the stratified flow (Fig. 13). According to Mertz and Wright (1992), the bottom pressure torque can be expressed as

$$\frac{1}{\rho_o} \nabla \times (P_b \nabla H) = \frac{1}{\rho_o} \nabla \times (\bar{P} \nabla H) - \nabla \times \left(\frac{\chi \nabla H}{H} \right), \quad (12)$$

where $\chi = g/\rho_0 \int_{-H}^0 z \rho dz$, and \bar{P} is the depth-averaged pressure gradient. By writing Eq. (12) in rotated coordinates locally aligned to the isobaths, Eq. (12) becomes

$$P_{y^*}^b = \bar{P}_{y^*} - \frac{\rho_0 \chi_{y^*}}{H}. \quad (13)$$

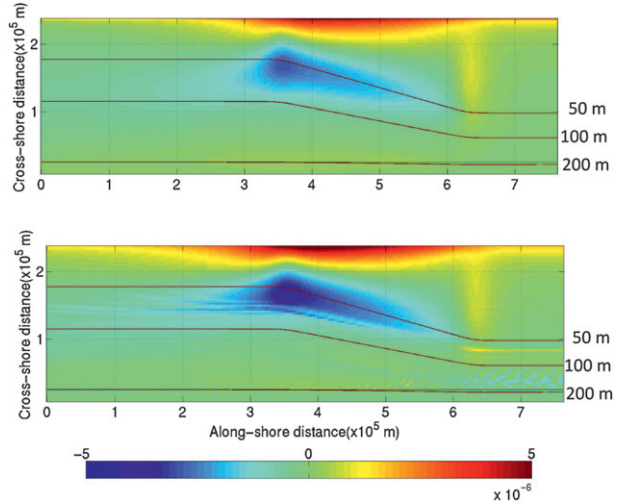


FIG. 14. Bottom stress curl ($10^{-6}, \text{ m}^2 \text{ s}^{-2}$) $-\nabla \times \tau_b$ for (top) non-stratified and (bottom) stratified flows on day 15.

It implies that the along-isobath bottom pressure gradient is equivalent to the depth-averaged along-isobath pressure gradient (first term on the right) and modulated by the JEBAR term (second term on the right) when flow is stratified. In NSCS during downwelling, the effect of the JEBAR on PY^* was generally weak (see below). The increase of PY^* (Fig. 13) in the stratified flow over the widened shelf was primarily due to the intensifications of the coastal downwelling jet and the associated shear vorticity (Fig. 12) on both sides of the jet over the central part of the widened shelf. This can also be shown by the high correlation between PY^* (Fig. 13) and PX^* (Fig. 15), in which both PY^* (cross-isobath current) and PX^* (along-isobath downwelling jet) elongated southeastward over the widened shelf.

b. Baroclinic PV balance

The baroclinic correction to the stratified flow due to density variation can be examined using the barotropic PV equation. The equation is obtained by taking curl of depth-average momentum equation (e.g., Haidvogel and Beckmann 1999),

$$\begin{aligned} \nabla \cdot \frac{\nabla \partial \Psi}{H} = & \nabla \times \frac{\int_{-H}^{\eta} NL dz}{H} + J \left(\frac{f}{H}, \Psi \right) + J \left(\chi, \frac{1}{H} \right) \\ & + \nabla \times \left(\frac{\tau_s}{\rho_o H} \right) - \nabla \times \left(\frac{\tau_b}{\rho_o H} \right). \end{aligned} \quad (14)$$

The term on the left side of Eq. (14) is the acceleration of PV. The terms on the right side are as follows: the first and second terms are PV advection; the third term is the JEBAR term; and the fourth and fifth terms are surface and bottom stress curls, respectively. The major balance

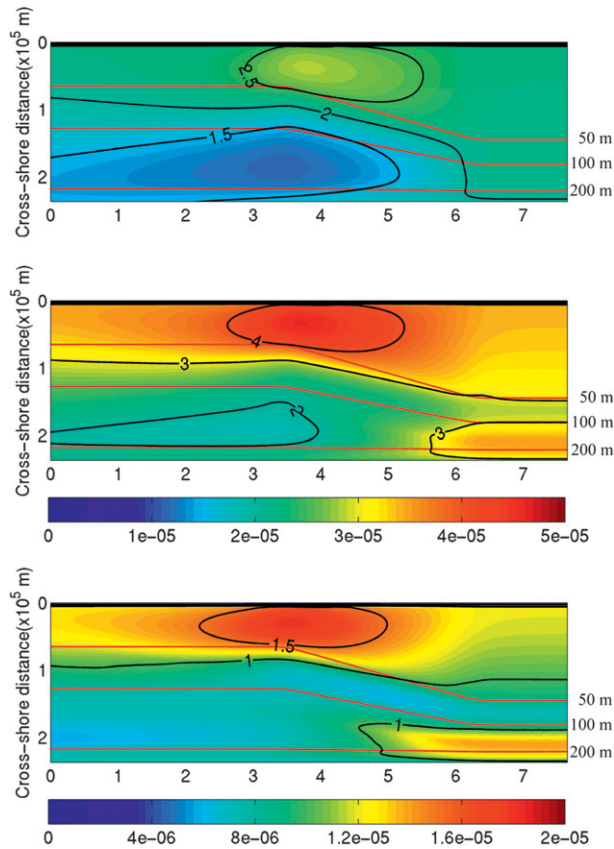


FIG. 15. Depth-integrated cross-isobath pressure gradient force (PX^* , $10^{-6} \text{ m}^2 \text{ s}^{-2}$) in the (top) nonstratified, (middle) stratified flows, and (bottom) the difference between PX^* (stratified flow) and PX^* (non-stratified flow) on day 15.

of Eq. (14) (Fig. 16) was generally between the PV advection and net PV dissipation by frictional curls. It was qualitatively similar to the barotropic PV balance (Fig. 6), although the magnitudes of the terms were larger in the stratified flow. By day 15, the acceleration term became very small. The nonlinear curl [term 2 in Eq. (14)] was generally small except at the head and tail of the widened shelf; its alternating positive/negative values or gain/loss of PV were consistent with the shoreward/seaward currents induced by nonlinear advection at the head/tail (Fig. 7). The JEBAR term was also about one order of magnitude smaller than the terms of the major balance, with the exception around the region along the 50-m isobath over the widened shelf where front was located (Fig. 10). Relatively large negative JEBAR may locally enhance the seaward transport. Positive JEBAR, farther offshore, played the opposite role. We found that the magnitude of the JEBAR had no dramatic change after day 10. The increase of seaward cross-isobath transport by the increase in PV advection/dissipation was several times larger than the JEBAR in this downwelling study, but the effect of

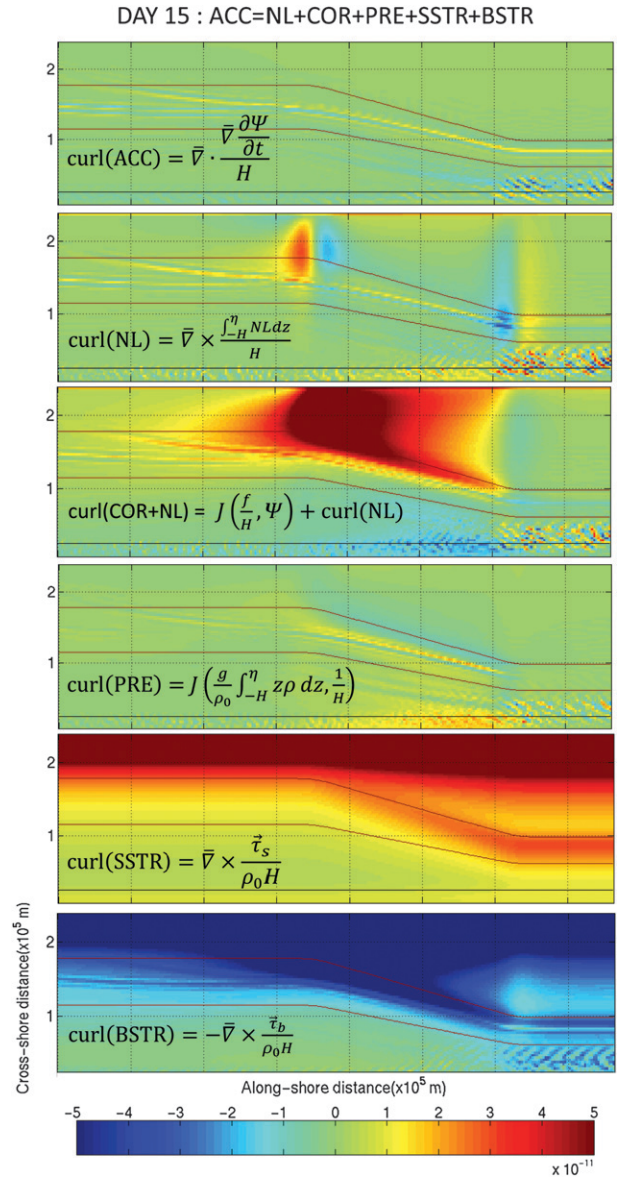


FIG. 16. (top to bottom) Vorticity acceleration, curl of nonlinear advection, advection of vorticity, the input of potential vorticity from wind stress curl, and the dissipation of vorticity by friction in the barotropic potential vorticity equation for stratified flow on day 15 ($10^{-11} \text{ s}^{-2} \text{ m}^{-1}$).

JEBAR may be greatly amplified when the crossing angle between isopycnal lines and isobaths becomes large (Gan and Qu 2008).

c. Contrasting transport

The importance of the stratification on the cross-isobath transport can be further illustrated by the contrasting component transport between stratified and non-stratified flow. By taking the curl of the depth-averaged

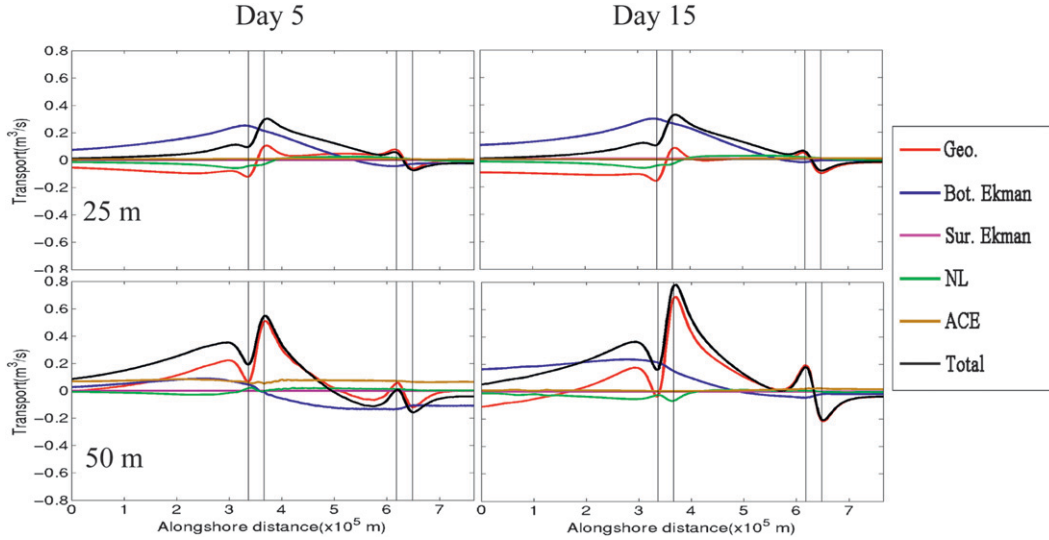


FIG. 17. Differences of depth-integrated transports ($\text{m}^3 \text{s}^{-1}$) across the isobaths 25 m (first row), and 50 m (second row) between the stratified and barotropic flow on days (left) 5 and (right) 15. Surface and bottom Ekman transports, nonlinear advection, and geostrophic currents contributed to the total transport differences. Negative values refer to the seaward transport. The areas between two pairs of vertical solid lines are the locations of the head and tail of the widened shelf. Two thin red rectangular boxes mark the region extending 35 km from the head and tail of the widened shelf.

momentum equation, the depth-averaged cross-isobath transport of Eq. (4) in the stratified flow becomes (Mertz and Wright 1992)

$$U^* = \frac{H^2 \left[\nabla \times \frac{\tau_b}{\rho_0 H} - \nabla \times \frac{\tau_s}{\rho_0 H} + \nabla \times \frac{\mathbf{V}\chi}{H} \right]}{fH_x}. \quad (15)$$

Equation (15) shows that the JEBAR term, acting like surface and bottom stresses, forces the flow across fH . As we showed before, the JEBAR effect on the cross-isobath transport of the downwelling flow in this study is much smaller than that arose from the bottom stress term in (15) when wind stress is absent. The invoked effect other than the one from the JEBAR was explored by simply finding the difference of each component in the cross-isobath transport between the stratified and nonstratified flows on day 5 during spinup and on day 15 when a quasi-steady state had been established (Fig. 17). Interestingly, the effect of stratification on the transport was obviously asymmetric in the along-isobath and cross-isobath directions, before and after the quasi-steady state. On both days 5 and 15, transports in the stratified flow differed from ones in the nonstratified flow mainly in T_g and T_b , and the responses of T_g and T_b to the stratification were not identical. In general, the spatial distribution of the total cross-isobath transports (T_t) in the nonstratified flow (Fig. 8) and the stratified flow (not shown) were

qualitatively similar in nature. The difference of T_g between stratified and nonstratified flow (defined as $\Delta T_g = T_{g\text{stratified}} - T_{g\text{nonstratified}}$), also had the same along-isobath pattern as the transport itself, but the pattern of the difference in T_b (defined as ΔT_b) was substantially different from the pattern of T_b itself. The depth-integrated T_s was independent of stratification although the surface Ekman velocity was enhanced (Lentz 2001; Gan et al. 2009b).

Along the 25-m isobath, the flows swiftly reached a steady state by day 5. ΔT_g was shoreward (negative) or stratified flow increased shoreward geostrophic transport on the western side of the head; it turned seaward (positive) at the eastern side of the head. Very similar condition occurred on day 15. Differently, ΔT_b was mainly positive with maximum value near the head, decreased away from the head and turned negative around the tail. These along-isobath variations of ΔT_g and ΔT_b amplified along the 50-m isobath. ΔT_g became strongly positive to the west of the widened shelf. On the other hand, ΔT_b was largely asymmetric on both sides of the head with positive at the western side and mainly negative values at the eastern side, respectively. Unlike what occurred in the shallower waters along the 25-m isobath, the stratified flow accelerated along the 50-m isobath on day 5, which led to an increase of seaward transport. By day 15, flows reached a quasi-steady state.

The processes that formed the differences are, in fact, associated with the flow field change over the entire

shelf by stratification, which may be better associated with changes in PX^* and PY^* . The increase of T_g was determined by the variations of the along-isobath pressure gradient or vorticity field in the stratified flow and the change in T_b was mainly associated with the intensity of the along-isobath current. These were, in turn, closely controlled by the change of the cross-isobath pressure gradient (ΔPX^*) by stratification. For example, $\Delta T_g < 0$ implies weaker negative PY^* in the stratified flow, while $\Delta T_b > 0$ indicates stronger alongshore velocity in the stratified flow. Both of them are connected with the intensity of downwelling jet or magnitude of ΔPX^* . In fact, the increase of PX^* around the head in stratified flow (Fig. 15) was because of increased intensity of confluence flow, in response to the increase of volume transport upstream of the widened shelf (east of the tail). Stratification weakened bottom friction and speeded up the inflow upstream of the widened shelf, as shown by negative ΔT_b in Fig. 17. The increased volume flux into the widened shelf gradually strengthened the intensity of the change in the along-isobath velocity or PX^* toward the head as the flow was converged by the narrowing shelf. When the flow speed exceeded the one in the nonstratified flow over the widened shelf, ΔT_b turned positive, reached maximum value at the head and decreased farther downstream. The positive ΔT_b may reduce the along-isobath velocity, which, in turn, creates the feedback effect between the friction layer and interior flow (Chapman and Lentz 1997) and subsequently thickens bottom friction layer to strengthen the along-isobath flow. However, the positive ΔPX^* (Fig. 15) suggested that the decrease of along-isobath flow by the increase of T_b could not offset the increase of along-isobath flow by the enhanced upstream volume flux input. The degree of shelf wideness or intensity of flow confluence largely controls the intensity of along-isobath flow or along-isobath PX^* . Indeed, these are the fundamental processes that lead to the intensified downwelling over the widened shelf: the T_t was determined by T_b and T_g , which were governed by the flow speed or PX^* and by associated shear vorticity or PY^* ; that is, by the intrinsic dynamics of flow-topography interactions over the widened shelf.

6. Summary and conclusions

Motivated by an observed intensified seaward cross-isobath transport over the widened shelf in the NSCS during downwelling, this study provided a general dynamics for the intensified cross-isobath transport over the shelf that varies in the alongshore direction. We utilized a three-dimensional circulation model over an idealized NSCS widened shelf, to identify the

process of this prominent coastal circulation and to validate the general dynamics in both nonstratified and stratified flows.

By the analyses that combined momentum balance with corresponding dynamics of the depth-integrated vorticity equation, we showed that the spatial strengthening of PV advection due to concurrent dissipation by net frictional stress curl over the widened shelf lead to the intensified downslope cross-isobath transport. Alternatively, the intensified transport was considered to be induced by the enhanced seaward cross-isobath geostrophic transport and bottom friction transport. It is found that the geostrophic cross-isobath transport is the dominant contributor to the intensified downslope transport in the downwelling circulation over the widened shelf; and the formation of the associated along-isobath pressure gradient force, PY^* , characterizes the unique process of flow-topography interaction for cross-isobath transport over the variable shelf topography.

Unlike the enhanced bottom Ekman transport over the widened shelf, dynamical rationalization for the formation of PY^* was not as obvious. Based on the depth-integrated vorticity dynamics, it was found that the vertically uniform PY^* was formed as a result of the net frictional stress curl in the water column. In the absence of the wind stress curl, the frictional stress curl was generated by the shear vorticity of the downwelling coastal jet. This finding naturally correlated the magnitude of PY^* with the topographically controlled PX^* that governed the intensity of the flow. The asymmetric topography over the widened shelf generated an elliptically shaped PX^* , which sustained the spatially variable downwelling jet, provided the shear vorticity for the formation of PY^* and governed the magnitude of the bottom frictional transport.

With a generally weak JBAR term due to well-mixed water during downwelling in this study, the effect of stratification on the downslope cross-isobath transport was mainly induced by PX^* increase because of the enhanced inflow upstream where bottom friction was diminished in the stratified flow. It asymmetrically changed the downslope cross-isobath transport in the along-isobath and cross-isobath directions, governed by the corresponding asymmetric response of vorticity and intensity of the downwelling jet over the widened shelf to the stratification-enhanced inflow upstream. It should be noted that the effect of JEBAR can be significant in many stratified shelves.

The general dynamics presented in this study necessitated the creation of a topographically controlled shelf circulation. Although it has qualitatively generality in the shelf circulation dynamics, the quantitative nature of the circulation may vary with different characteristic

conditions of shelf, such as its length scale, magnitude of forcing, and strength of stratification.

Acknowledgments. This research was supported by the National Key Basic Research Development Program 2009CB421208 and Hong Kong's Research Grant Council under Project GRF601008 and GRF601007. The authors are grateful for the helpful suggestions provided by two anonymous reviewers.

APPENDIX

Bottom Pressure Gradient Force

Equations (7) and (10) of bottom pressure gradient force will be derived here. We start with the depth-integrated form of a steady linearized two-dimensional momentum equation:

$$f \int_{-H}^0 \begin{pmatrix} -v \\ u \end{pmatrix} dz = -\frac{1}{\rho_0} \int_{-H}^0 \begin{pmatrix} P_x \\ P_y \end{pmatrix} dz + \frac{\tau_s}{\rho_0} - \frac{\tau_b}{\rho_0}. \quad (\text{A1})$$

Using a horizontal curl,

$$\bar{\nabla} \times = \begin{pmatrix} -\frac{\partial}{\partial y} \\ \frac{\partial}{\partial x} \end{pmatrix},$$

on both sides of Eq. (A1), the Coriolis term becomes $f[(\int_{-H}^0 u dz)_x + (\int_{-H}^0 v dz)_y]$ on an f plane and vanishes because of the conservation of volume. Using the chain rule, the pressure gradient term is differentiated to give two terms:

$$-\frac{1}{\rho_0} \int_{-H}^0 \begin{pmatrix} -\frac{\partial}{\partial y} \\ \frac{\partial}{\partial x} \end{pmatrix} \cdot \begin{pmatrix} P_x \\ P_y \end{pmatrix} dz - \frac{1}{\rho_0} \begin{pmatrix} -H_y \frac{\partial}{\partial H} \\ H_x \frac{\partial}{\partial H} \end{pmatrix} \cdot \int_{-H}^0 \begin{pmatrix} P_x \\ P_y \end{pmatrix} dz. \quad (\text{A2})$$

The first term of (A2) vanishes. The second term is the bottom pressure torque $-1/\rho_0(-H_y P_x^b + H_x P_y^b)$. By choosing the direction of $y = y^*$ to be the along-isobath direction at the point being analyzed, the result is

$$-\frac{1}{\rho_0} (H_{x^*} P_{y^*}^b) + \bar{\nabla} \times \left(\frac{\tau_s}{\rho_0} - \frac{\tau_b}{\rho_0} \right) = 0. \quad (\text{A3})$$

This also holds true for a baroclinic ocean.

Now we turn to the case of including nonlinear advection in a barotropic ocean. Nonlinear advection can be rewritten by the identity

$$\begin{pmatrix} uu_x + vv_y \\ uv_x + vu_y \end{pmatrix} = \bar{\nabla} \left(\frac{\|\mathbf{v}\|^2}{2} \right) + \xi \begin{pmatrix} -v \\ u \end{pmatrix}.$$

Equation (A1) becomes

$$H \bar{\nabla} \left(\frac{\|\mathbf{v}\|^2}{2} \right) + H(f + \xi) \begin{pmatrix} -v \\ u \end{pmatrix} = \frac{-1}{\rho_0} \int_{-H}^0 \begin{pmatrix} P_x \\ P_y \end{pmatrix} dz + \frac{\tau_s}{\rho_0} - \frac{\tau_b}{\rho_0}, \quad (\text{A4})$$

where ξ is the vorticity, $v_x - u_y$. Applying a horizontal curl gives

$$J \left(H, \frac{\|\mathbf{v}\|^2}{2} \right) + uH\xi_x + vH\xi_y = \frac{-1}{\rho_0} (-H_y P_x^b + H_x P_y^b) + \bar{\nabla} \times \left(\frac{\tau_s}{\rho_0} - \frac{\tau_b}{\rho_0} \right). \quad (\text{A5})$$

Rotating the rectangular coordinates so that $y = y^*$ is along-isobath, and then dividing H_{x^*} on both sides, results in Eq. (10) becoming

$$\frac{-1}{\rho_0} P_{y^*}^b = \frac{1}{H_{x^*}} \bar{\nabla} \times \left(\frac{\tau_b}{\rho_0} - \frac{\tau_s}{\rho_0} \right) + \frac{1}{H_{x^*}} J(\psi, \xi) + \left(\frac{\|\mathbf{v}\|^2}{2} \right)_{y^*}. \quad (\text{A6})$$

REFERENCES

- Allen, J. A., and P. A. Newberger, 1996: Downwelling circulation on the Oregon continental shelf. Part I: Response to idealized force. *J. Phys. Oceanogr.*, **26**, 2011–2035.
- Chapman, D. C., and S. J. Lentz, 1994: Trapping of a coastal density front by the bottom boundary layer. *J. Phys. Oceanogr.*, **24**, 1464–1479.
- , and —, 1997: Adjustment of stratified flow over a sloping bottom. *J. Phys. Oceanogr.*, **27**, 340–356.
- Gan, J., and J. S. Allen, 2002: A modeling study of shelf circulation off northern California in the region of the Coastal Ocean Dynamics Experiment: Response to relaxation of upwelling winds. *J. Geophys. Res.*, **107**, 3184, doi:10.1029/2001JC001190.
- , and T. Qu, 2008: Coastal jet separation and associated flow variability in the southwest South China Sea. *Deep-Sea Res. I*, **55**, 1–19.
- , J. S. Allen, and R. Samelson, 2005: On open boundary conditions for a limited-area coastal model off Oregon. Part 2:

- Response to wind forcing from a regional mesoscale atmospheric model. *Ocean Modell.*, **8** (1–2), 155–173.
- , A. Cheung, X. G. Guo, and L. Li, 2009a: Intensified upwelling over a widened shelf in the northeastern South China Sea. *J. Geophys. Res.*, **114**, C09019, doi:10.1029/2007JC004660.
- , L. Li, D. X. Wang, and X. G. Guo, 2009b: Interaction of a river plume with coastal upwelling in the northeastern South China Sea. *Cont. Shelf Res.*, **29**, 728–740.
- Haidvogel, D. B., and A. Beckmann, 1999: *Numerical Ocean Circulation Modeling*. Imperial College Press, 318 pp.
- Janowitz, G. S., and L. J. Pietrafesa, 1982: The effects of alongshore variation in bottom topography on a boundary current—(topographically induced upwelling). *Cont. Shelf Res.*, **1**, 123–141.
- Lentz, S. J., 2001: The influence of stratification on the wind-driven cross-shelf circulation over the North Carolina shelf. *J. Phys. Oceanogr.*, **31**, 2749–2760.
- , R. T. Guza, S. Elgar, F. Feddersen, and T. H. C. Herbers, 1999: Momentum balances on the North Carolina inner shelf. *J. Geophys. Res.*, **104**, 18 205–18 226.
- MacCready, P., and P. B. Rhines, 1991: Slippery bottom boundary layers on a slope. *J. Phys. Oceanogr.*, **23**, 5–22.
- Mellor, G. L., and T. Yamada, 1982: Development of a turbulence closure model for geophysical fluid problems. *Rev. Geophys.*, **20**, 851–875.
- Mertz, G., and D. G. Wright, 1992: Interpretations of JEBAR term. *J. Phys. Oceanogr.*, **22**, 301–305.
- Niller, N. P., 1969: On the Ekman divergence in an oceanic jet. *J. Geophys. Res.*, **74**, 7048–7052.
- Pringle, J. M., 2002: Enhancement of wind-driven upwelling and downwelling by alongshore bathymetric variability. *J. Phys. Oceanogr.*, **32**, 3101–3112.
- Shchepetkin, A. F., and J. C. McWilliams, 2005: The regional oceanic modeling system (ROMS): A split-explicit, free-surface, topography following-coordinate oceanic model. *Ocean Modell.*, **9**, 347–404.
- Weisberg, R. H., R. He, Y. Liu, and J. I. Virmani, 2005: West Florida shelf circulation on synoptic, seasonal, and interannual time scales. *Circulation in the Gulf of Mexico: Observations and Models*, *Geophys. Monogr.*, Vol. 161, Amer. Geophys. Union, 325–347.

Copyright of Journal of Physical Oceanography is the property of American Meteorological Society and its content may not be copied or emailed to multiple sites or posted to a listserv without the copyright holder's express written permission. However, users may print, download, or email articles for individual use.